Science
AAAS

Biscrolling Nanotube Sheets and Functional Guests into Yarns
Márcio D. Lima, *et al.*
Science **331**, 51 (2011);
DOI: 10.1126/science.1195912

Science (print ISSN 0036-8075; online ISSN 1095-9203) is published weekly, except the last week in December, by the American Association for the Advancement of Science, 1200 New York Avenue NW, Washington, DC 20005.

Biscrolling Nanotube Sheets and Functional Guests into Yarns

Márcio D. Lima, Shaoli Fang, Xavier Lepró, Chihye Lewis, Raquel Ovalle-Robles, Javier Carretero-González, Elizabeth Castillo-Martínez, Mikhail E. Kozlov, Jiyoung Oh, Neema Rawat, Carter S. Haines, Mohammad H. Haque, Vaishnavi Aare, Stephanie Stoughton, Anvar A. Zakhidov, Ray H. Baughman*

Multifunctional applications of textiles have been limited by the inability to spin important materials into yarns. Generically applicable methods are demonstrated for producing weavable yarns comprising up to 95 weight percent of otherwise unspinnable particulate or nanofiber powders that remain highly functional. Scrolled 50-nanometer-thick carbon nanotube sheets confine these powders in the galleries of irregular scroll sacks whose observed complex structures are related to twist-dependent extension of Archimedean spirals, Fermat spirals, or spiral pairs into scrolls. The strength and electronic connectivity of a small weight fraction of scrolled carbon nanotube sheet enables yarn weaving, sewing, knotting, braiding, and charge collection. This technology is used to make yarns of superconductors, lithium-ion battery materials, graphene ribbons, catalytic nanofibers for fuel cells, and titanium dioxide for photocatalysis.

Powders of particles or nanofibers are well-known additives for introducing new and improved functionality into yarns, and the importance of this area motivates new advances (*1*–*3*). Current methods use additive dispersion in a fiber matrix or incorporation on fiber surfaces, but problems remain: (i) powder loading levels are typically low, (ii) nanoparticle and nanofiber functionality can degrade when processing decreases accessible surface area, and (iii) powders on yarn surfaces can lack durability. Powders are rarely spinnable into yarns without changing basic structure; a notable exception is solution (*4*, *5*) and solid-state spun (*6*–*12*) carbon nanotubes (CNTs). Strong, weavable multifunctional yarns could be seamlessly integrated into intelligent clothing, structural textiles, and woven electrodes that are flexible, durable, and hierarchically engineered in porosity by yarn weaving, thereby providing advantages over conventional multifunctional film and bulk composites. Our goal is to spin porous multifunctional yarns in which a low concentration of strong host enables weavability, flexibility, and durability, while a high guest concentration adds functions such as energy storage, harvesting, and conversion.

Fabrication of biscrolled yarns. Our approach involves twist-based spinning of CNT sheets (the host) that are overlaid with a layer of up to 99 weight percent (wt %) of one or more other functional materials (the guest). We will scroll guest-host bilayers into a biscrolled yarn in which a minor CNT sheet concentration confines guest powders in down to nanometer-scale proximity in scroll galleries. The composition of biscrolled yarns is denoted X% guest@host$_{i,j}$, where X is the wt % of guest in the yarn and subscripts i and j denote the number of host sheet stacks under and over the guest layer, respectively.

Unless otherwise noted, the host sheets were drawn from carbon multiwalled nanotube (MWNT) forests grown by chemical vapor deposition (CVD). The forest height was typically ~350 μm, and the nanotubes had an outer diameter of ~9 nm and contained ~6 walls. Forest-drawn CNT sheets (*7*) were overlaid with the guest and then twist-spun using methods that, in some cases, are like those for making pure CNT yarns (*6*–*12*). The as-drawn CNT sheets have remarkable structure and properties (*6*, *7*, *13*) that are useful for making biscrolled yarns. Although these sheets are aerogels having a carbon network density (~1.5 mg/cm^3) close to that of air and an areal density of only about 1 to 3 μg/cm^2, they have a high specific strength (i.e., strength normalized by density) of up to 144 MPa cm^3/g (*7*). Densification decreases sheet thickness to as low as 50 nm and increases nanotube direction sheet specific strength to 560 MPa cm^3/g, compared with ~125 MPa cm^3/g for the Mylar and Kapton used for ultralight air vehicles (*7*). Using an approximate density of 0.8 g/cm^3 for the densified sheet, the unnormalized strengths for the nanotube sheet and the Mylar and Kapton are 450 MPa and 175 MPa.

Biscrolling begins with fabrication of a guest/host stack by depositing guest material onto (i) a

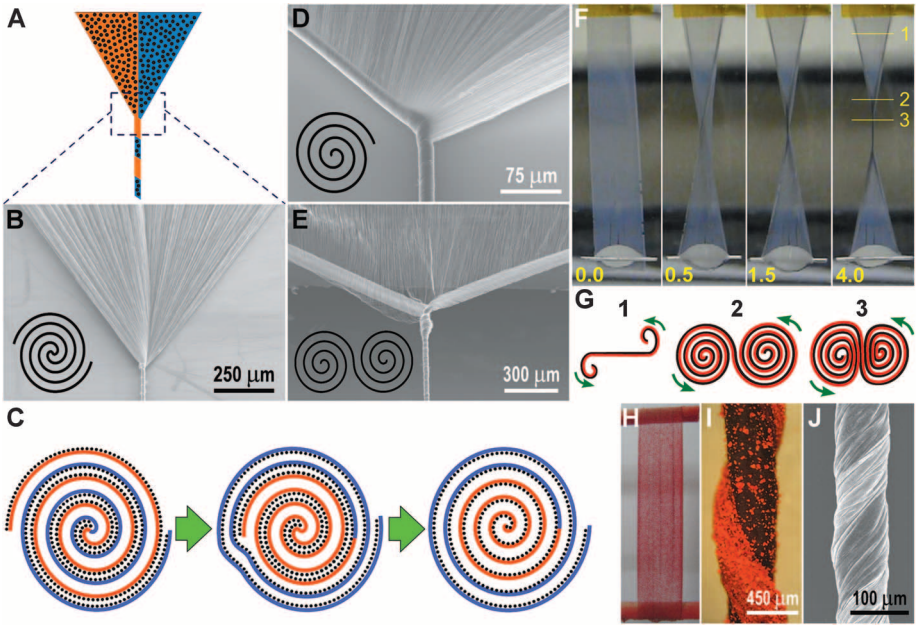

Fig. 1. (**A**) Illustration of biscrolling by twist insertion in a spinning wedge, where black dots represent guest particles. (**B**) SEM micrograph of Fermat-type twist insertion during spinning from a MWNT forest. The inset illustrates a Fermat scroll. (**C**) Illustration of evolution from a Fermat scroll to an Archimedean scroll. (**D** and **E**) SEM images of guest-free spinning wedges showing Archimedean (D) and dual Archimedean (E) scrolls, which are illustrated in the insets. (**F**) Sequential photographs of liquid-state twist insertion in a 1-cm-wide MWNT sheet that is coated with filtration-deposited 92 wt % boron nitride nanotube guest. The number of inserted turns is shown at the bottom of each photograph. (**G**) Illustration of the expected cross sections at the positions marked in (F). (**H** and **I**) Photographs of a 1-cm-wide, bilayered stack fabricated by electrostatic deposition of a commercial red paint powder on a single MWNT sheet (H) and a biscrolled yarn made by dry-state twist insertion in a stack of eight MWNT sheets that was similarly electrostatically coated with this dry red paint (I) (*14*). (**J**) SEM image of a 70% Ti@MWNT$_{2,0}$ biscrolled yarn produced by symmetrically inserting twist in a rectangular bilayer sheet that is rigidly supported in a liquid bath. The Ti guest was deposited by electron beam evaporation.

The Alan G. MacDiarmid NanoTech Institute, University of Texas at Dallas, Richardson, TX 75083, USA.

*To whom correspondence should be addressed: E-mail: ray.baughman@utdallas.edu

CNT sheet wedge directly produced by twist-based spinning from a forest (Fig. 1, A, B, and D) or (ii) forest-drawn CNT sheets (Fig. 1, E and F) (*14*). Guest deposition onto a CNT web using an electrostatic powder coating gun is fast and controllable due to attraction between charged guest particles and the oppositely charged web (Fig. 1, H and I) (*14*). Other liquid-free guest deposition processes include electron beam evaporation (Fig. 1J), sputtering, and aerosol filtration (Fig. 2, E and F) (*14*). Liquid-based guest deposition also works, like using a MWNT sheet stack as a filter to capture liquid-dispersed, CVD-synthesized (*15*) boron nitride (BN) nanotubes (Fig. 1F), electrophoretic deposition, and ink-jet printing (*14*). Ink-jet printing of guest can be used for even a single self-supported MWNT sheet having 1 $\mu g/cm^2$ areal density and enables patterned depositions of guest—thereby producing engineered variation in guest composition along the yarn length and diameter (movie S3). In the liquid filtration method, MWNT sheets are placed on a filter membrane; liquid-dispersed particles/nanofibers are deposited on the nanotube sheets by filtration; the resulting bilayer guest/host stack on the filter membrane is cut into a strip, attached to end supports, and mounted in a liquid bath, where the filter membrane is dissolved so that twist can be inserted (Fig. 1F and fig. S3) (*14*).

The process for biscrolled yarn fabrication ends with twisting a bilayer guest/sheet stack to make yarn. The amount of inserted twist was typically selected so that the yarn bias angle (the angle between yarn direction and the orientation direction of helically wrapped nanotubes on the outer yarn surface) was between about 30° and 45° (*14*). Although use of such large twist angles does not maximize tensile strength for guest-free yarn, it provides high compressive forces that are useful for confining guest powders in biscrolled yarns.

Biscrolling can be easily extended from CNT host to electrically insulating hosts such as SiO_2 and Si_3N_4 nanotubes (*14*). Individual CNTs and CNT bundles in free-standing, forest-drawn MWNT sheets were conformally coated with from 4-nm- to 18-nm-thick SiO_2 or Si_3N_4 by plasma-enhanced CVD. Both ceramic-coated CNT sheets and derived ceramic nanotube sheets, with CNT cores oxidatively removed, were twist-spun to make yarns (fig. S5D), and both can be overlaid with other functional materials to enable the spinning of biscrolled yarns (*14*). Figure 3, A and B, shows a Si_3N_4NT@$MWNT_{0,2}$ biscrolled yarn made by twist-based spinning a stack of Si_3N_4NT sheets and solid-state-drawn MWNT sheets. Conformally coating MWNTs in MWNT sheets with ~18-nm thickness of Si_3N_4 does not appreciably affect the in-plane sheet conductance or the conductance of derived twisted yarns.

Structure development and transitions for scrolled and biscrolled yarn. Can we find ways to dramatically modify yarn structure, so that future efforts can optimize yarn properties by structure manipulation? Toward this goal, we have discovered that fundamentally different nanotube yarn structures are produced by changing spinning conditions and resulting parameters (such as end constraints, stress asymmetry during spinning, spinning-wedge base width, and "wedge angle," the total apex angle where the wedge converges to yarn) (*14*). The observed structures (Figs. 1 and 2) are related to Archimedean and Fermat spirals and more complicated interconnected spirals. Accordingly, ignoring the radial dependence of interlayer spacings, we name structures observed for biscrolled and guest-free yarns as Archimedean, Fermat, and dual Archimedean scrolls. "Archimedean" means that a sheet edge is buried deep in a scroll, and "dual Archimedean" means that sheet edges are buried in different interconnected scrolls, like in two dimensions for a Cornu spiral (Fig. 1, E and G) (*16*).

In Fermat biscrolling (or Fermat scrolling for a guest-free yarn), the twist process starts from the center of a symmetric spinning wedge, as shown in Fig. 1, A and B. The edges of the spinning wedge wrap (i.e., scroll) in opposite directions around the thereby formed scroll core (Fig. 1B and fig. S2A), so that both wedge edges are exterior in the final yarn. Asymmetry in the stress applied to opposite sides of the spinning wedge can displace the core of the Fermat scroll from the center of the spinning wedge, so that one edge of the spinning wedge twists on top of the other, thereby burying this latter edge in an unbalanced Fermat scroll, as illustrated in Fig. 1C. If the scroll core is moved to a wedge edge (Fig. 1D and fig. S2B), scroll unbalancing is complete and an Archimedean scroll results. Because they have similar geometry, we approximate a highly unbalanced Fermat scroll by an Archimedean scroll and a largely balanced Fermat scroll as a Fermat scroll. Like a hanging curtain that is bunched at the bottom to form a wedge, use of a large wedge angle introduces pleats for Fermat scrolling and asymmetric Archimedean scrolling (Fig. 1, B and D, and fig. S2B) because of the need to incorporate the base width in a wedge width that decreases as the wedge apex is approached (*14*).

Spinning a rectangular sheet strip under constant load is more complicated than continuous spinning from a forest-derived wedge, for which we have observed only formation of single Fermat scrolls, single Archimedean scrolls, and intermediate states between these extremes. Twist of a rectangular sheet starts with sheet folding that is origami-like, except that plastic sheet deformation occurs. This folding repeats during subsequent rotations to form a new system of folds until two spinning wedges are obtained. Subsequently, for symmetric twisting, two interconnected Archimedean scrolls form for each spinning wedge, which are centered on the folds located at wedge edges (Fig. 1F and movie S1). These Archimedean scrolls are ultimately twisted together as in two-ply yarn (Fig. 1, F, G, I, and J). Because the guest is exterior to the MWNT sheet for one scroll and interior for the second, the barber-pole–like structure of Fig. 1, I and J, arises

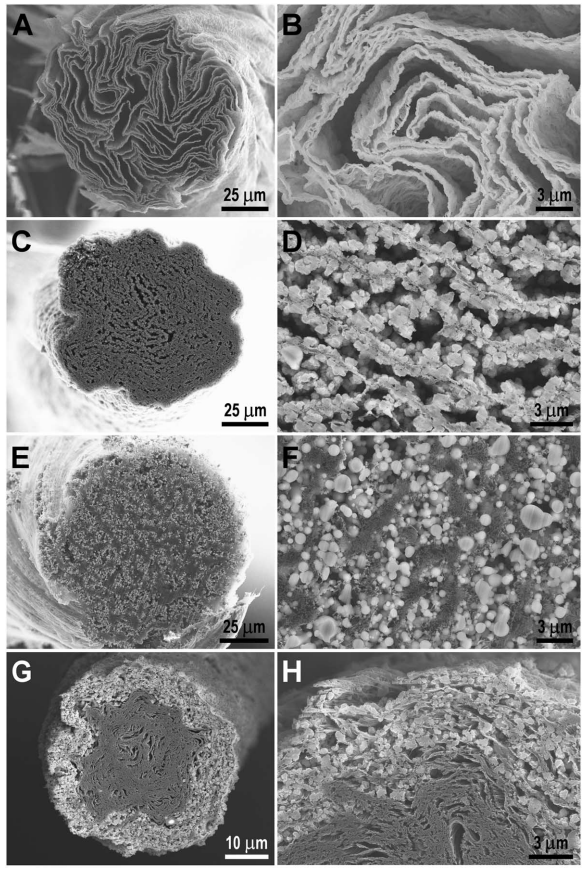

Fig. 2. SEM images of the cross sections of biscrolled yarns. (**A** and **B**) 70% Ti@$MWNT_{2,0}$ yarn fabricated by guest deposition using electron beam evaporation (25 nm Ti) and symmetrical twist insertion in liquid. (**C** and **D**) 93% TiO_2@$MWNT_{2,1}$ yarn made by filtration-based guest deposition and symmetrical twist in liquid. (**E** and **F**) TiO_2@$MWNT_{2,0}$ yarn made by aerosol-based guest deposition and twist insertion in air. (**G** and **H**) TiO_2@$MWNT_{2,1}$ yarn made by patterned filtration-based guest deposition on MWNT sheets and asymmetrical twist insertion in liquid. The patterned deposition was limited to a strip along the sheet's edge spanning 15% of its width.

in the final yarn. Conversely, applying sufficiently asymmetric loads to opposite sides of the bilayered sheet (by using nonparallel supporting rods) produces a single Archimedean scroll (*14*), with either the host or guest side of the bilayer exterior to the yarn.

The absence of observed Fermat scrolling for twisting a short rectangular sheet strip or bilayer stack between rigid supports (in either liquid or air) and the absence of observed formation of two interconnected Archimedean scrolls during continuous spinning from a forest wedge can be attributed to change from a rigid end support to one that enables partial relief of twist-generated strain. In fact, if we symmetrically twist a rectangular sheet strip that is rigidly supported at one end and connected to a nanotube forest at the opposite end, the generated spinning wedge on the forest end shows Fermat scrolling and the spinning wedge attached to the rigid support shows formation of dual Archimedean scrolls.

Scanning electron microscopy (SEM) images of the cross sections obtained by cutting biscrolled yarns with a focused Ga ion beam reveals the gallery structure that confines the guest (Fig. 2). The biscrolled yarns in Fig. 2, A to F, result from twisting a rectangular sheet stack between rigid supports, and in each case the macroscopically observed twist process is dual Archimedean. This interpretation is supported by the barber-pole–type structure of Fig. 1J for the biscrolled yarn of Fig. 2, A and B. If we coat only 15% of the sheet with guest (adjacent to one sheet edge) and asymmetrically apply twist so that formation of a single Archimedean scroll is macroscopically observed, the yarn structure of Fig. 2, G and H, results. As expected for a single Archimedean scroll that starts from the guest-free side of the wedge, an inner core of scrolled guest-free nanotube sheet is surrounded by an outer sheath having guest particles in host galleries. Figure 3, A and B, show lateral and cross-sectional views for a biscrolled yarn obtained by dry-state twist insertion in a rectangular stack consisting of MWNT sheets on top of Si_3N_4 nanotube (Si_3N_4NT) sheets (*14*).

Biscrolled yarns made by all-dry processing can have low densities and high void volume fraction (F_{void}, exterior to the nanotube bundles and guest), which enable SEM imaging of particles deep inside the yarn (Fig. 3C for TiO_2@$MWNT_{1,0}$). The guest particles interfere with twist-based densification, and dry processing avoids densification caused by liquid surface tension. For instance, the density of dry-processed 50% TiO_2@$MWNT_{1,0}$ yarn is only 0.19 g/cm^3 (F_{void} = 0.91), compared with 0.8 g/cm^3 (F_{void} = 0.42) for guest-free, dry-spun MWNT yarn and 0.7 g/cm^3 (F_{void} = 0.79) for liquid-state processed 93% TiO_2@$MWNT_{2,1}$ yarn (Fig. 2, C and D) (*14*). Despite the very low density and high void volume fraction for 50% TiO_2@$MWNT_{1,0}$ yarn, the specific strength for this dry-state fabricated yarn is ~200 MPa cm^3/g (Fig. 4A).

Why are the galleries of host and guest so complicated and irregular (Fig. 2, A to H) when the images in Fig. 1 clearly show scrolling and biscrolling processes that are structurally related to three-dimensionally extended Fermat, Archimedean, or dual Archimedean spiral geometries? One reason is that scroll cores formed during the initial stages of biscrolling have low density, and yarn densification during the final stages of twist insertion involves layer buckling and plastic deformation. Another reason is that yarn densification by joining pleat sidewalls can look in yarn cross-section like layer branching and termination. Origami-like folding of a rectangular sheet during wedge formation increases complexity, as does the collapse of dual Archimedean spirals as they are plied together (Fig. 1, G, I, and J). Structural irregularity also results from layer buckling and yarn shape distortion due to surface-tension–induced yarn densification during wet-state processing and variations in the size and shapes of large-diameter guest particles.

Processability and strength of biscrolled yarns. Even when a very small amount of CNT host mechanically confines an otherwise unbonded powder guest, biscrolled yarns can be knotted and sewn, as indicated by the images in Fig. 3, D to F. Experiments also show that a biscrolled yarn containing 93 wt % TiO_2 can be attached to a textile and washed in an ordinary washing machine without measurable (>2 wt %) loss of the guest or change in the strength (~50 MPa cm^3/g) of the biscrolled yarn (*14*).

We use two types of specific strength to describe mechanical properties: "specific strength" and "MWNT specific strength," which correspond to the breaking force divided by the total linear yarn density and the linear density of the MWNTs in the yarn, respectively. Specific strengths can be more reliable than usual strength measurements, because errors in yarn cross-sectional area are avoided. Figure 4A results for TiO_2 particles deposited from an aerosol (*14*) (movie S2) show that the yarn specific strength decreases approximately linearly with increasing wt % TiO_2, reaching 120 MPa cm^3/g for 76% TiO_2@MWNT. This strength retention and the ability of the host nanotubes to confine guest nanoparticles results from long MWNT lengths and the known (*7*) self-weaving within CNT sheets.

Applications potential of multifunctional biscrolled yarns. Superconducting yarn was obtained by biscrolling a mixture of magnesium and boron powders as guest on MWNT sheets (*14*). One percent CNT host held 99 wt % of these precursors during twist insertion and harsh chemical treatment, despite the large B and Mg particle diameters (~40 μm) compared with the ~50-nm thickness for densified MWNT sheet. Yarn stability during conversion of this guest to superconducting MgB_2 by exposure to highly corrosive Mg vapor (750°C for 30 min in Ar) indicates the ability of the MWNT host to confine the guest in chemical and thermal environments where most materials degrade. Four-probe electrical conductivity measurements (Fig. 4B) show that the biscrolled yarn becomes superconducting at the expected critical temperature (39 K) for MgB_2 (*17*). This method for making superconducting yarn avoids the more than 30 drawing steps needed to produce millimeter-diameter, iron-clad superconducting wires from

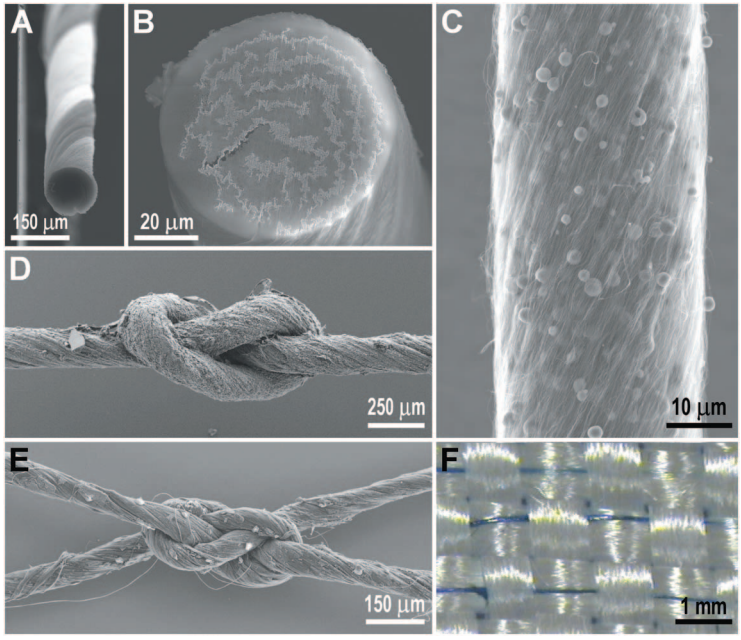

Fig. 3. (**A** and **B**) SEM images of Si_3N_4NT@$MWNT_{0,2}$ biscrolled yarn that was twist-spun in air. The brighter areas correspond to MWNTs. (**C**) SEM image of TiO_2@$MWNT_{1,0}$ yarn made by aerosol-based guest deposition and twist insertion in air. (**D**) SEM image of overhand knot in 95% $LiFePO_4$@$MWNT_{3,3}$ yarn. (**E**) SEM image of carrick bend knot between two 88% SiO_2@$MWNT_{3,0}$ yarns. (**F**) Photograph of 85% TiO_2@$MWNT_{3,0}$ yarn that has been hand sewn into Kevlar (DuPont) textile.

Mg/B/MWNT precursor using the powder-in-tube method (*18*).

Biscrolled yarns containing up to 98 wt % graphene oxide nanoribbons in 2 wt % MWNT host were made and then converted to graphene nanoribbon yarn by reducing the graphene oxide nanoribbons (*14*). The graphene oxide nanoribbons were synthesized by minor modification of Tour's method (*19*), which involves longitudinally unzipping MWNTs in an oxidizing mixture of $KMnO_4$ in aqueous H_2SO_4 (*14*). The specific strength of biscrolled yarn containing 70 wt % of unoriented graphene oxide nanoribbons reached 95 MPa cm^3/g, which is higher than for graphene oxide sheets (68 MPa cm^3/g) (*20*). Conversion of the graphene oxide nanoribbon guest to graphene nanoribbons by thermal annealing the yarn (900°C in 5% H_2 in argon) did not appreciably change specific strength, although yarn weight decreased by 57 wt %. The high reported Li^+ storage capacity of graphene oxide nanoribbons (*21*) suggests that biscrolled graphene nanoribbon yarns may be used as weavable anodes for flexible Li-ion batteries.

The performance of biscrolled yarns as flexible battery cathodes was evaluated by using $LiFePO_4$ as guest, which is an inexpensive, environmentally friendly, high-performance Li-ion battery cathode material (*22*, *23*). Charge collection from this high-rate, high-capacity redox material is an important problem because of its low electronic conductivity, and the nanoscale proximity between highly conducting MWNT host and the $LiFePO_4$ in biscrolled yarns should provide a solution to this problem that minimizes total electrode weight.

A biscrolled yarn with 98.5 wt % $LiFePO_4$ guest exhibited an unexpectedly high gravimetric electrical conductivity of 8 S cm^2/g (*14*). The corresponding gravimetric conductivity based on the mass/length ratio of host MWNT (~530 S cm^2/g) is within experimental error of that for a twist-spun MWNT yarn that does not contain guest (410 S cm^2/g), indicating that guest inclusion does not degrade electrical transport by the host MWNTs. This high gravimetric electrical conductivity means biscrolled yarn cathodes do not require the commonly used aluminum current collector, conducting additive, and binding agent that can increase electrode weight over 30%.

The electrode results of Fig. 4C are for a 100-μm-diameter biscrolled yarn containing 95 wt % $LiFePO_4$ guest, which is weavable and knottable (Fig. 3D) despite this massive powder concentration (*14*). Based on total electrode weight, reversible charge storage capabilities of 115 mAh/g at C/3 rate and 99 mAh/g at 1C were obtained, where a C/3 rate is the discharge rate needed to release one-third of the theoretical storage capacity of $LiFePo_4$ (170 mAh/g) in 1 hour. An impressive capacity of 146 mAh/g at 1C rate (based on $LiFePO_4$ weight) has been reported for a $LiFePO_4$/MWNT/binder composite sheet (*24*), which reduces to 105 mAh/g when based on estimated total electrode weight (including a likely 20 wt % Al foil current collector, such as those found in commercial $LiFePO_4$ batteries). Using Li metal as the anode and the total cathode weight to provide normalization for energy and power densities, energy storage densities of 379 Wh/kg and 135 Wh/kg resulted for power densities of 180 W/kg and 4590 W/kg, respectively. By plying together such a biscrolled yarn cathode and biscrolled yarn anode (e.g., graphene nanoribbon guest), a Li-ion battery that is a single two-ply yarn could be made, such as those demonstrated for supercapacitors using solution-spun CNT yarns (*25*).

Because catalytic oxygen reduction is crucial for fuel cells and metal-air batteries, and the cost of noble metal catalysts is a major problem, we next investigated whether nitrogen-doped MWNT (N_xMWNT) guest in biscrolled yarns can provide this catalysis. Although N_xMWNT is known to be a promising oxygen-reduction catalyst (*26*–*29*), the question is, "Can this catalytic activity be retained in a biscrolled yarn that is weavable into a strong, flexible cathode?" Evidence for catalytic activity was obtained by comparing the cyclic voltammetry of 91% MWNT@MWNT and 90% N_xMWNT@MWNT biscrolled yarns that were identically fabricated except for replacing undoped MWNT guest with N_xMWNT. The N-doped MWNTs (N/C ~ 0.03) were prepared using a floating catalyst method and purified to remove iron catalyst (*14*, *30*). Figure 4D shows that the onset potential for oxygen reduction by N_xMWNT@MWNT shifts by ~0.3 V with respect to that for MWNT@MWNT. The same shift in onset potential was observed for the bilayer sheet stack that was precursor to the N_xMWNT@MWNT yarn, indicating that biscrolling is not interfering with catalytic activity.

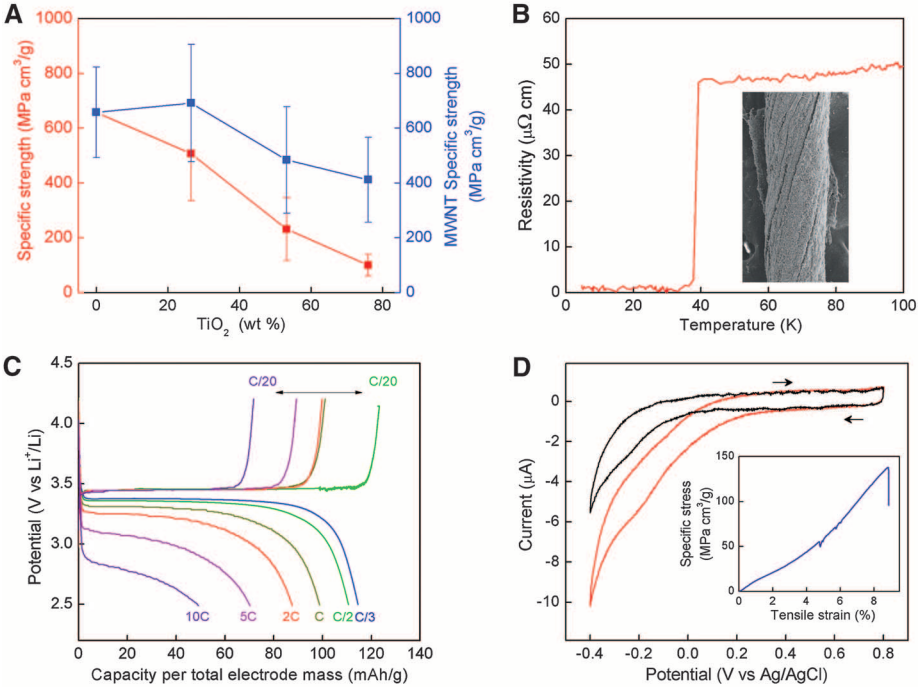

Fig. 4. (**A**) Specific strength and MWNT specific strength of TiO_2@$MWNT_{2,0}$ yarn as a function of TiO_2 loading, showing ±1 SD error bars (for $N \geq 4$ per data point). The biscrolled yarn was made by deposition of TiO_2 from a chemically produced aerosol and dry-state twist insertion into a rectangular bilayer sheet. (**B**) Electrical resistivity versus temperature for superconducting MgB_2@$MWNT_{2,1}$ yarn, showing T_c = 39 K. (Inset) SEM image of the 170-μm-diameter yarn. (**C**) Galvanostatic charge-discharge curves versus charge level (per total weight of electrode) for a 95% $LiFePO_4$@$MWNT_{4,6}$ yarn using different discharge rates. (**D**) Cyclic voltammetry at 5 mV/s for a 90% N_xMWNT@$MWNT_{1,0}$ yarn (red curve) and 91% MWNT@$MWNT_{1,0}$ yarn (black curve) in oxygen-saturated 0.5 M H_2SO_4, showing a voltage shift in the onset for oxygen reduction due to catalysis by the N-doped MWNTs. (Inset) Specific stress versus tensile strain for 70% N_xMWNT@$MWNT_{1,2}$ yarn.

Summary. We show that a minute amount of MWNT host web enables twist-based spinning of yarn from diverse powders and nanofibers, while maintaining guest functionality. The mechanical properties of these webs enables weavability, knottability, and durability for biscrolled yarns containing up to at least 95 wt % guest, which can result in applications for wearable electronic textiles and for strong woven electrodes of batteries and fuel cells. Using patterned deposition for bilayer stacks, TiO_2 guest can be located in the sheath of a biscrolled yarn, thereby optimizing light absorption for such applications as self-cleaning textiles and Graetzel solar cells. The ability to make biscrolled yarns having Fermat, Archimedean, and dual Archimedean scroll geometries can be exploited to optimize yarn properties. The demonstrated use of CNT sheets as removable templates for making spinnable sheets of other nanotubes extends biscrolling to new hosts and provides a route to other types of nanotube yarns.

References and Notes

1. D. Li, Y. Xia, *Adv. Mater.* **16**, 1151 (2004).
2. H. Ye, H. Lam, N. Titchenal, Y. Gogotsi, F. Ko, *Appl. Phys. Lett.* **85**, 1775 (2004).
3. M. J. Uddin *et al.*, *J. Photochem. Photobiol. Chem.* **199**, 64 (2008).
4. B. Vigolo *et al.*, *Science* **290**, 1331 (2000).
5. M. E. Kozlov *et al.*, *Adv. Mater.* **17**, 614 (2005).
6. M. Zhang, K. R. Atkinson, R. H. Baughman, *Science* **306**, 1358 (2004).
7. M. Zhang *et al.*, *Science* **309**, 1215 (2005).
8. X. Zhang *et al.*, *Adv. Mater.* **18**, 1505 (2006).
9. Q. Li *et al.*, *Adv. Mater.* **18**, 3160 (2006).
10. X. Zhang *et al.*, *Small* **3**, 244 (2007).
11. L. Xiao *et al.*, *Appl. Phys. Lett.* **92**, 153108 (2008).
12. Y. Nakayama, *Jpn. J. Appl. Phys.* **47**, 8149 (2008).
13. A. E. Aliev *et al.*, *Science* **323**, 1575 (2009).
14. Materials and methods are available as supporting material on *Science* Online.
15. D. Golberg, Y. Bando, C. Tang, C. Zhi, *Adv. Mater.* **19**, 2413 (2007).
16. V. M. Castaño, *Jpn. J. Appl. Phys.* **44**, 5009 (2005).
17. J. Nagamatsu, N. Nakagawa, T. Muranaka, Y. Zenitani, J. Akimitsu, *Nature* **410**, 63 (2001).
18. S. X. Dou *et al.*, *Adv. Mater.* **18**, 785 (2006).
19. D. V. Kosynkin *et al.*, *Nature* **458**, 872 (2009).
20. D. A. Dikin *et al.*, *Nature* **448**, 457 (2007).
21. T. Bhardwaj, A. Antic, B. Pavan, V. Barone, B. D. Fahlman, *J. Am. Chem. Soc.* **132**, 12556 (2010).
22. A. K. Padhi, K. S. Nanjundaswamy, J. B. Goodenough, *J. Electrochem. Soc.* **144**, 1188 (1997).
23. J. Chen, M. S. Whittingham, *Electrochem. Commun.* **8**, 855 (2006).
24. X. Li, F. Kang, X. Bai, W. Shen, *Electrochem. Commun.* **9**, 663 (2007).
25. A. B. Dalton *et al.*, *Nature* **423**, 703 (2003).
26. K. Gong, F. Du, Z. Xia, M. Durstock, L. Dai, *Science* **323**, 760 (2009).
27. S. Kundu *et al.*, *J. Phys. Chem. C* **113**, 14302 (2009).
28. S. Maldonado, K. J. Stevenson, *J. Phys. Chem. B* **109**, 4707 (2005).
29. Y. Shao, J. Sui, G. Yin, Y. Gao, *Appl. Catal. B* **79**, 89 (2008).
30. M. Terrones, R. Kamalakaran, T. Seeger, M. Rühle, *Chem. Commun. (Camb.)* **23**, 2335 (2000).

31. We thank A. L. Elias and M. Terrones for N-doped MWNTs; D. Goldberg and Y. Bando for boron nitride nanotubes; E. J. Kneeland, A. E. Nabinger, S. Y. Yoon, and M. J. de Andrade for help with experiments; and A. E. Aliev and D. M. Rogers for useful comments. Supported by Air Force Grant AOARD-10-4067, Air Force Office of Scientific Research grants FA9550-09-1-0384 and FA9550-09-1-0537, Office of Naval Research Multidisciplinary University Research Initiative grant N00014-08-1-0654, NSF grant DMI-0609115, and Robert A. Welch Foundation grant AT-0029. Some of the authors have filed patent application PCT/US2010/36378 (27 May 2010).

Supporting Online Material

www.sciencemag.org/cgi/content/full/331/6013/51/DC1
Materials and Methods
Figs. S1 to S7
References
Movies S1 to S3

2 August 2010; accepted 26 November 2010
10.1126/science.1195912

The Origins of Hot Plasma in the Solar Corona

B. De Pontieu,[1]* S. W. McIntosh,[2] M. Carlsson,[3] V. H. Hansteen,[3,1] T. D. Tarbell,[1] P. Boerner,[1] J. Martinez-Sykora,[1,3] C. J. Schrijver,[1] A. M. Title[1]

The Sun's outer atmosphere, or corona, is heated to millions of degrees, considerably hotter than its surface or photosphere. Explanations for this enigma typically invoke the deposition in the corona of nonthermal energy generated by magnetoconvection. However, the coronal heating mechanism remains unknown. We used observations from the Solar Dynamics Observatory and the Hinode solar physics mission to reveal a ubiquitous coronal mass supply in which chromospheric plasma in fountainlike jets or spicules is accelerated upward into the corona, with much of the plasma heated to temperatures between ~0.02 and 0.1 million kelvin (MK) and a small but sufficient fraction to temperatures above 1 MK. These observations provide constraints on the coronal heating mechanism(s) and highlight the importance of the interface region between photosphere and corona.

A wide variety of theoretical models to explain the heating of the solar corona have been proposed since the discovery in the corona of emission from ions that are formed at temperatures of several million kelvin (MK) (*1*). These models range from energy deposition through the damping of magnetohydrodynamic waves, to nanoflares (*2*) that arise when the magnetic field is stressed (via reconnection) (*3*). Despite decades of effort to determine which mechanism dominates, the lack of detailed observations of the fundamental heating process has hampered progress. Instead, most efforts have focused on statistical approaches that study the dependence of the heating mechanism on magnetic field strength, loop length, or plasma density (*4*), or that are based on assumptions about unresolved individual heating events (*5*).

Spicules are phenomena that have held particular promise as discrete coronal heating events (*6*, *7*). The chromospheric mass flux that these jets propel to coronal heights is estimated to be two orders of magnitude larger than the mass flux of the solar wind (*8*). Although they have been observed in a variety of chromospheric and transition region (TR) lines (*9*, *10*), a coronal counterpart has not been observed. As a result, a role for spicules in coronal heating has been dismissed as unlikely (*8*). On the other hand, recent observations have revealed a new type of spicule that is shorter-lived (~100 s) and more dynamic (~50 to 100 km/s) than its classical counterpart (*10*, *11*). Recently, a spatiotemporal correlation between chromospheric brightness changes, suggestively linked to these "type II" spicules, and coronal upflows of 50 to 100 km/s, deduced from spectral line asymmetries of coronal lines at the footpoints of loops, was found (*12*). This statistical relationship suggests that the chromospheric jets may play a substantial role in providing the corona with hot plasma, but a detailed one-to-one correlation between spicules and their coronal counterparts has remained elusive (*10*, *11*, *13*).

We exploited the recent detection of the disk counterpart of type II spicules: rapid blueshifted events (RBEs), which are observed in chromospheric lines such as Hα 6563 Å (*14*, *15*). Observations suggest evidence for acceleration and heating along their long axis before they rapidly fade out of the chromospheric passbands, which may indicate heating to TR temperatures (*15*). We used coordinated observations of RBEs in the blue wing of Hα (–0.868 Å or –41 km/s) with the Narrowband Filter Imager of the Solar Optical Telescope (SOT) (*17*) onboard the Hinode solar physics mission (*16*), and found direct evidence of a strong correlation of RBEs with short-lived brightenings in a wide range of TR and coronal passbands observed with the Atmospheric Imaging Assembly (AIA) onboard the recently launched Solar Dynamics Observatory (SDO). Using an automated detection code, we found 2434 RBEs occurring in the active-region plage footpoints of coronal loops during a 1-hour-long time series (*18*) on 25 April 2010 (Fig. 1 and fig. S1).

RBEs form rapidly and often recur in the same position (Fig. 2). They become visible as an absorbing feature in the upper chromospheric Hα line that is blueshifted by 40 to 60 km/s along the line of sight (*18*). A little bit later, brightenings occur in the vicinity of the leading edge of the RBE in the He II 304 Å, Fe IX 171 Å, and Fe XIV 211 Å AIA passbands (Fig. 2). These passbands are dominated by lines from ions that are formed at temperatures of 0.1, 0.8, and 2 MK, respectively (*18*). The extreme ultraviolet emission moves at velocities similar to those of the leading end of the RBE, although the emission in He II 304 Å (and sometimes Fe IX 171 Å) often,

[1]Lockheed Martin Solar and Astrophysics Laboratory, 3251 Hanover Street, Organization ADBS, Building 252, Palo Alto, CA 94304, USA. [2]High Altitude Observatory, National Center for Atmospheric Research, Post Office Box 3000, Boulder, CO 80307, USA. [3]Institute of Theoretical Astrophysics, University of Oslo, Post Office Box 1029 Blindern, 0315 Oslo, Norway.

*To whom correspondence should be addressed. E-mail: bdp@lmsal.com